Extreme phonon anharmonicity underpins superionic diffusion and ultralow thermal conductivity in argyrodite Ag₈SnSe₆

Qingyong Ren^{1,2,3#}, Mayanak K. Gupta^{4,5#}, Min Jin⁶, Jingxuan Ding⁴, Jiangtao Wu¹, Zhiwei Chen⁷, Siqi Lin^{6,7}, Oscar Fabelo⁸, Jose Alberto Rodríguez-Velamazán⁸, Maiko Kofu⁹, Kenji Nakajima⁹, Marcell Wolf¹⁰, Fengfeng Zhu¹¹, Jianli Wang^{12,13}, Zhenxiang Cheng¹³, Guohua Wang¹, Xin Tong^{2,3}, Yanzhong Pei^{7*}, Olivier Delaire^{4,14,15*}, Jie Ma^{1*}

- 1. Key Laboratory of Artificial Structures and Quantum Control, School of Physics and Astronomy, Shanghai Jiao Tong University, 800 Dongchuan Road, 200240 Shanghai, China.
- 2. Institute of High Energy Physics, Chinese Academy of Sciences, Beijing 100049, China.
- 3. Spallation Neutron Source Science Center, Dongguan 523803, China.
- 4. Department of Mechanical Engineering and Materials Science, Duke University, Durham, NC 27708, USA
- 5. Solid State Physics Division, Bhabha Atomic Research Centre, Trombay, Mumbai 400085, India
- 6. College of Materials, Shanghai Dianji University, Shanghai 201306, China
- 7. Interdisciplinary Materials Research Center, School of Materials Science and Engineering, Tongji University, Shanghai 201804, China
- 8. Institut Laue-Langevin, 38042 Grenoble Cedex 9, France
- 9. J-PARC Center, Japan Atomic Energy Agency, Tokai, Ibaraki 319-1195, Japan
- 10. Technische Universität München, Heinz Maier-Leibnitz Zentrum (MLZ), Lichtenbergstraße 1, 85748 Garching, Germany
- 11. Jülich Centre for Neutron Science (JCNS) at Heinz Maier-Leibnitz Zentrum (MLZ), Forschungszentrum Jülich, Lichtenbergstrasse 1, D-85747 Garching, Germany
- 12. College of Physics, Jilin University, Changchun 130012, China
- 13. Institute for Superconducting and Electronic Materials, University of Wollongong, Squires Way, North Wollongong, Australia
- 14. Physics Department, Duke University, Durham, NC 27708, USA
- 15. Chemistry Department, Duke University, Durham, NC 27708, USA
- # These authors equally contributed to the work.
- * Corresponding authors: yanzhong@tongji.edu.cn, olivier.delaire@duke.edu, jma3@sjtu.edu.cn

Abstract

Ultralow thermal conductivity and fast-ionic diffusion endow superionic materials with excellent performance both as thermoelectric converters and as solid-state electrolytes. Yet, the correlation and interdependence between these two features remain unclear owing to a limited understanding of their complex atomic dynamics. Here, we investigate ionic diffusion and lattice dynamics in argyrodite Ag₈SnSe₆ using synchrotron X-ray and neutron scattering techniques along with machine-learned molecular dynamics. We identify a previously-missed critical interplay of vibrational dynamics of mobile Ag and host framework that controls the overdamping of low-energy Ag-dominated phonons into a liquid-like quasielastic response enabling superionicity. Concomitantly, the persistence of long-wavelength transverse acoustic phonons across the superionic transition challenges a proposed "liquid-like thermal conduction" picture. Rather, striking thermal broadening of low-energy phonons, starting even below 50 K, reveals extreme phonon anharmonicity and weak bonding as underlying features of the potential energy surface responsible for the ultralow thermal conductivity (<0.5 W m⁻¹ K⁻¹) and fast diffusion. Our results provide new fundamental insights into complex atomic dynamics in superionic materials for energy conversion and storage.

Superionic solids represent an intermediate state of matter between ordered crystal and disordered liquid phases, simultaneously exhibiting long-range ordering and short-range disordering characteristics on distinct sublattices¹. They are usually built on a rigid framework structure with large connected interstitial spaces, in which weakly-bonded ions may either order on shallow-potential minima or delocalize with liquid-like diffusivities². Superionic materials tend to exhibit ultralow lattice thermal conductivity while the rigid framework structure supports electrical transport, enabling excellent thermoelectric performance³⁻⁵. Many studies over the past decade attempted to expose the atomistic mechanisms underlying the ultralow lattice thermal conductivity in superionic thermoelectric materials, including weak chemical bonding and low sound velocity⁶, large unit cell and low cutoff of acoustic phonons⁴, strong phonon anharmonicity or selective breakdown of phonon quasiparticles⁷⁻⁹, rattling-like phonon damping¹⁰, liquid-like heat propagation^{3, 11, 12}. In the latter scenario, a disappearance of shear recovery force suppresses the heat transport channel associated to transverse acoustic phonons. However, such a scenario remains challenged as the suppression of transverse phonon branches in liquid would require a characteristic ionic jump time comparable to or shorter than the phonon relaxation time^{8, 13}.

Superionic materials are also intensively investigated for their superior ionic conductivity, as candidate solid-state electrolytes for potentially safer all-solid-state batteries^{14, 15}. A major direction in the design of high-performance solid-state superionic conductors is to reduce the ionic migration energy barriers ^{16, 17}, yet strategies involve enlarged lattice volume and open bottleneck^{18, 19}, disordered and distorted local coordination²⁰, concerted migration²¹, as well as various point defects²². The common idea behind these approaches is to regulate the complex interactions between the cation and anion sublattices in superionic conductors, or from the perspective of lattice dynamics, the phonon-ion interactions^{23, 24}. Toward rationalizing ionic transport, new inquiries have focused on the lattice dynamics. It was found that lattice softness and polarizability²⁵, paddle-wheel-like rotation of polyanionic units¹, low average phonon frequency of the lithium sublattice²⁶, as well as strong phonon anharmonicity^{27, 28} could play important roles in facilitating ionic transport. However, detailed studies of lattice dynamics in superionic conductors remain limited. A deeper understanding is highly desirable, for instance to chart how phonon anharmonicity influences ionic diffusion and whether ionic diffusion is modulated by some average overall phonon frequency or by more specific modes^{23, 26, 27, 29}.

A major obstacle toward clarifying the lattice dynamics of superionic materials lies in the challenge of crystal-structure characterization owing to the existence of complex, correlated disordering and diverse phase transitions^{5, 20}. The desirability for theoretical simulations with larger length scales and longer time scales also brings a tremendous challenge to conventional first-principles simulations²⁴. In addition, the need for large single crystals often precluded the direct measurement of the four-dimensional phonon dispersions and dynamical structure factor using inelastic neutron scattering (INS), limiting previous studies to powder-averaged data in which a lot of valuable information can be lost^{8, 12, 26, 27, 29}. These challenges have impeded our understanding of ultralow lattice thermal conductivity and the establishment of a clear physical picture of the coupling of atomic dynamics and ion transport in superionic solids.

Herein, we report a comprehensive study on the argyrodite-type Ag_8SnSe_6 superionic thermoelectric material, simultaneously exhibiting a lattice thermal conductivity as low as ~0.2 W m⁻¹ K⁻¹ and an ionic conductivity reaching up to ~1 S m⁻¹ near the phase transition temperature^{30, 31}. The complex crystalline structure of Ag_8SnSe_6 was probed with in-situ synchrotron X-ray diffraction (SXRD), single crystal neutron diffraction (SCND) and analyzed with pair-distribution function (PDF) and maximum entropy methods (MEM). Vibrational and diffusive dynamics were

revealed via INS and quasi-elastic neutron scattering (QENS) measurements facilized with machine-learned molecular dynamics (MLMD) simulations. These momentum and energy resolved scattering measurements and simulations enable us to comprehensively map the microscopic spatio-temporal correlations of atoms responsible for bulk transport properties. A fast diffusion signal clearly emerges above the superionic transition and increases with temperature, concomitant with an obvious change in the peak position and width of low-energy phonon modes, revealing a direct correlation between the dynamics of the lattice and those of mobile ions. Further analysis of the single-crystal phonon dispersions in the low energy range demonstrates the critical interplay between the Ag migration and motion of so-called free Se ions, which controls overdamping of the Ag sublattice resulting in diffusive behavior. Strikingly, measurements performed down to very low temperatures reveal a drastic anharmonic broadening of spectral features in the phonon density of states (DOS) starting even below 50 K. It is therefore the extremely soft and anharmonic potential energy landscape, rather than fast ionic jumps, that leads to the ultralow lattice thermal conductivity.

Results

Ag sublattice melting through superionic phase transition. The in-situ SXRD patterns from 90 K to 450 K, collected on the Powder Diffraction beamline, Australian Synchrotron, are shown in Figs. 1a,b. A sharp phase transition occurs at T_c ~355 K from the low-T orthorhombic phase $(Pmn2_1, denoted with 'O')$ to the high-T cubic phase $(F\overline{4}3m, denoted with 'C')$ (Fig. 1c) with a tiny unit cell volume expansion by 0.077 Å^3 (or by 0.0225 %). Combined with latent heat and thermal hysteresis as observed from differential scanning calorimetry (DSC) measurements, it demonstrates a first order nature of this phase transition. Above T_c, the SXRD background exhibits a broad bump in the range of ~2 to ~3 Å⁻¹ around the scattering vector of {331} planes, implying a partial disordering of the crystal structure (Fig. 1b). More detailed crystal structures and irregular atomic distributions were analyzed with SCND data by means of MEM (see Supplementary Section 1)32. The volumic nuclear density distributions from MEM are shown in Figs. 1d,f, and Figs. 1e,g compare the density maps in the (011)_c plane of the O phase, matching the (111)_c plane of the C phase (Supplementary Fig. 4a). Clearly, Ag atoms in the O structure are constrained to vibrate around localized potential energy minima, although their spatial displacements are already quite large, reflecting a shallow potential. On the other hand, the C phase exhibits continuous Ag distributions forming an interconnected percolation path (also see Supplementary Fig. 4), indicating that the bump feature in the SXRD background in Figs. 1a,b results from the delocalized Ag ions on their sublattice above T_c . This change in the Ag sublattice across the superionic transition is reproduced by our MLMD simulations in the right panels of Figs. 1e,g as well as the PDF analysis in Supplementary Fig. 5.

Abnormal behaviors of the 'free-Se' atoms. Further analysis on the crystal structure evolution across the phase transition is given in Supplementary Section 2. The comparison between the O and C phases in Supplementary Fig. 6 shows that the positions of Sn and Se atoms follow a one-to-one correspondence between the two phases. The transformations of Se4₀ $(2a) \rightarrow \text{Se2}_{\text{C}}(4c)$ and Se5₀ $(2a) \rightarrow \text{Se1}_{\text{C}}(4a)$ present larger and abrupt position shifts as well as larger increases in the atomic displacement parameters (ADPs) than other Se atoms bonded to Sn $(\text{Se1}/2/3_{\text{O}} \rightarrow \text{Se3}_{\text{C}})$ (also see the dark-blue arrows in Supplementary Fig. 4a and Supplementary Figs. 7,8). To understand the abnormal behaviors in the Se4₀ $(\rightarrow \text{Se2}_{\text{C}})$ and Se5₀ $(\rightarrow \text{Se1}_{\text{C}})$ ions, the atomic environments were carefully revisited for the C phase in Supplementary Fig. 9. The

continuously distributed Ag clusters are supported and separated by the Se atoms. In turn, Se1_c (4a) and Se2_c (4c) are surrounded and isolated by the Ag clusters and referred to as "free Se", while Se3_c (16e) atoms are strongly bonded to Sn1_c (4b). The unconstrained environment enables the large shifts and ADPs of these free Se ions across the superionic transition. We explain below how the displacement of these ions is key to enable long-range diffusion in the superionic C phase.

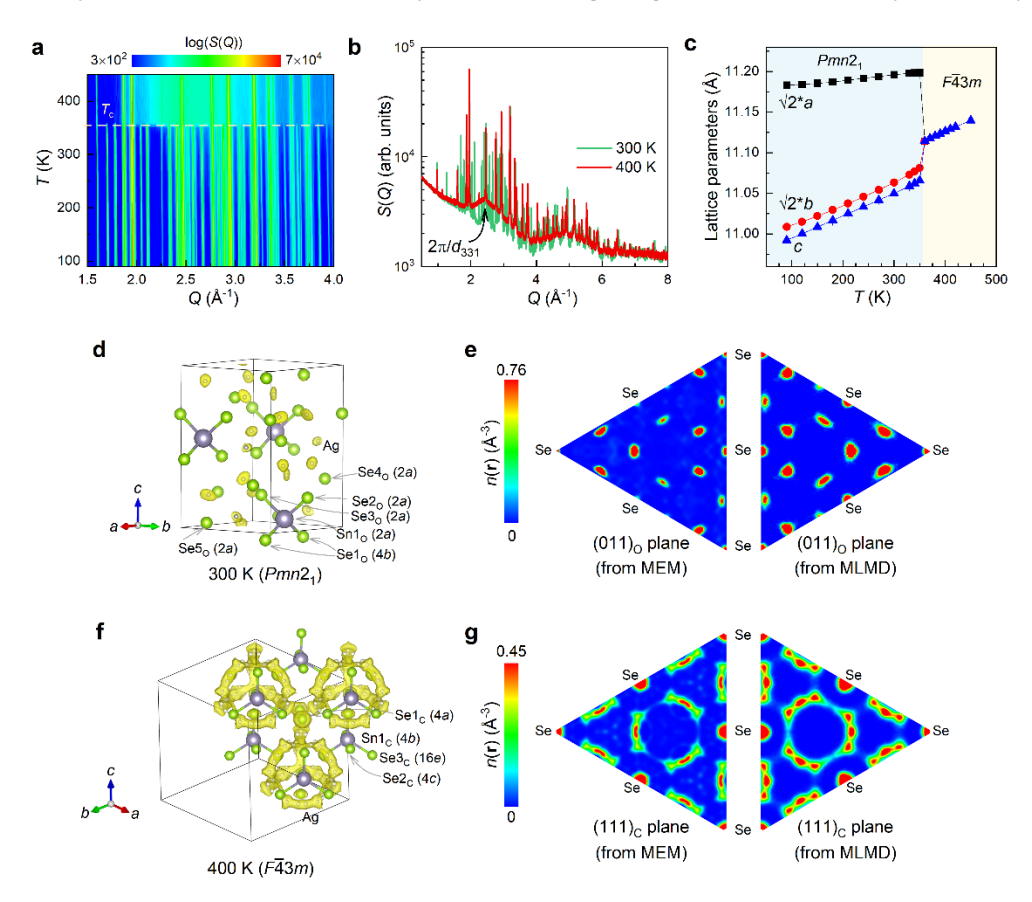


Fig. 1 Crystal structures and phase transition in Ag₈SnSe₆. a, Contour image of the synchrotron X-ray diffraction (SXRD) patterns, S(Q), over 90-450 K. b, SXRD patterns at 300 K and 400 K. Obvious bumps around the scattering vector of {331} planes are present in the background above the phase transition temperature of T_c ~355 K. c, Variation of the lattice parameters with increasing temperature as extracted from the SXRD data. d-g, Schematic of the crystal structures at (d,e) 300 K and (f,g) 400 K as determined from the analysis of single crystal neutron diffraction (SCND) data. The sample has orthorhombic ($Pmn2_1$, denoted with 'O') and cubic ($F\overline{4}3m$, denoted with 'C') structures at 300 K and 400 K, respectively. The Wyckoff position notations are given after the atomic names. Yellow iso-surfaces in (d,f) represent the nuclear density distributions of the atoms in the unit cells as calculated from the observed structure factor (SCND data) employing the maximum entropy method (MEM). Nuclear density maps in (e) (011)0 plane of the orthorhombic structure and (g) (111)c plane in the cubic structure, the left panel determined from MEM analysis, and the right panel comes from the machine-learned molecular dynamics simulations (MLMD). It is noted that the $(011)_0$ plane matches the $(111)_c$ plane (see Supplementary Fig. 4a). All the continuous and extended nuclear density distributions in (e,g) come from delocalized Ag atoms except the areas marked for Se atoms. More details about the crystal structures are given in Supplementary Fig. 9.

Strong correlation between lattice dynamics and ionic diffusion. The analysis of the averaged (static) crystal structures based on our diffraction measurements revealed an extended, continuous distribution of Ag ions above the superionic transition. To gain deeper insights into the superionic phase transition, we tracked the lattice dynamics as a function of temperature with INS measurements using time-of-flight spectroscopy (Methods). First, the orientation-averaged dynamic structure factors, S(Q,E), were collected on powder samples. Figures 2a,b show S(Q,E)obtained with an incident energy of E_i = 9.09 meV collected on the TOFTOF spectrometer at 300 and 410 K, respectively. Clear acoustic phonon dispersion streaks are observed in the 300 K spectrum (Fig. 2a), for example, emanating from the Bragg peak around 2.5 $^{-1}$, and merging with optical phonon branches that develop a flat horizontal band around 2.8 meV. On the other hand, a quasielastic continuum emerges in the vicinity of the elastic line (near E = 0 meV) at 410 K (Fig. 2b). This quasi-elastic neutron scattering (QENS) signal, widely used to study the ion-diffusion dynamics^{8, 24}, is very strong and exhibits a considerable broadening in energy. It becomes so broad that it strongly overlaps with the acoustic-phonon vertical streaks and the flat phonon bands around 2.8 meV (Supplementary Fig. 10), making it challenging to visually distinguish the latter two scattering signals, although the data analyses in the following prove their existence underneath the QENS signal.

The evolution of low-frequency dynamics across the superionic transition is further investigated by integrating S(Q,E) over the Q range of [2.0, 2.4] \mathring{A}^{-1} (Fig. 2c). Below T_C , a distinct peak is present around 2.8 meV with a clear energy gap from the elastic line. This peak contains the top of acoustic phonon dispersions away from the zone center as well as a bundle of flat lowenergy optical branches (Supplementary Fig. 10). At low T, this peak can be approximated with a single damped harmonic oscillator (DHO) function, although it represents many closely-spaced branches (Supplementary Fig. 11a). However, an additional Lorentzian profile centered at E=0 is required to obtain a good fit above T_c (Supplementary Fig. 11b), which is the expected QENS component reflecting the fast diffusion in the superionic phase. We find that the flat phonon band (2.8 meV peak at low T) gradually softens and broadens from 150 K to 350 K and subsequently becomes nearly constant above T_c , where its width becomes larger than its center energy, characteristic of an overdamped regime (Fig. 2d). This evolution indicates that the emergence the diffusive behavior is strongly correlated to the overdamping of the low-energy phonons. This trend across the superionic transition is successfully reproduced with our MLMD calculations as shown in Fig. 2e. In addition, the computed partial dynamic structure factors (Supplementary Fig. 12) establish that the diffusive (QENS) component of the INS spectra mainly stems from the Ag atoms. Long-range diffusion is also confirmed with the QENS analysis in a smaller Q range, and the fit of the QENS width to the FWHM = $2\hbar DQ^2$ formula yields a long-range diffuse coefficient of $D = 13.5 \times 10^{-6}$ cm² s⁻¹ at 400 K which is in fair agreement with our mean squared displacements (MSD) analysis based on MLMD simulations (see Supplementary Section 4), confirming superionic character.

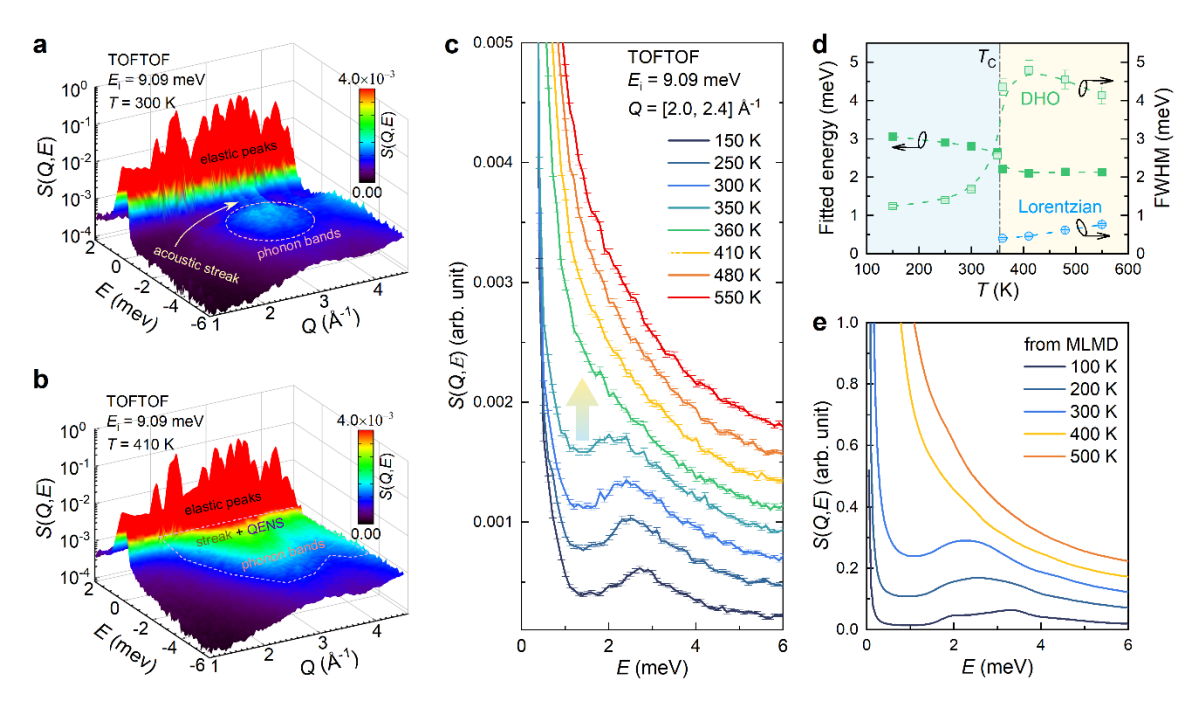


Fig. 2 Lattice and diffusive dynamics across the superionic transition. a,b, Surface plots of the dynamic structure factor, S(Q,E), of polycrystalline Ag_8SnSe_6 sample at **(a)** 300 K and **(b)** 410 K, collected on the TOFTOF spectrometer with an incident neutron energy of $E_i = 9.09$ meV. The signal saturated red comes from elastic scattering, including Bragg peaks and transmission signal, while acoustic phonon streak, acoustic & optical phonon bands and QENS signals are marked with arrow or dashed lines. **c**, Sliced S(Q,E) curves over the Q range of [2.0, 2.4] \mathring{A}^{-1} for all temperatures collected at TOFTOF. The arrow indicates a sharp change in the dynamics across the transition. **d**, Fitted energy of the damped harmonic oscillator function (DHO, solid symbols), and the full width at half maximum (FWHM) of the DHO and Lorentzian profiles (open symbols) as determined from the spectral fitting of the sliced S(Q,E) data (Supplementary Fig. 11). The dashed lines are a guide for the eyes. **e**, S(Q,E) from MLMD simulations at different temperatures across the phase transition.

Mode-resolved evolution of coupled dynamics of Ag^+ ions and framework. To get a deeper mode-resolved understanding of the interplay between host lattice vibrations and Ag diffusion, we analyze the single-crystal INS spectra in the (*HHL*) plane (Supplementary Figs. 15a-d in Supplementary Section 5) from the AMATERAS spectrometer. In particular, the transverse phonons along the [00/] direction in the (440) Brillouin zone were obtained at 300 and 450 K as illustrated in Figs. 3a,b (see Supplementary Fig. 19 for longitudinal phonons along [*hh*0]). The transverse acoustic (TA) phonon branches can be clearly tracked below and above T_C from the constant-Q spectra in Figs. 3c,d, although the phonon peaks are slightly broadened above T_C . This indicates that long-wavelength acoustic phonon quasiparticles remain well defined in the superionic state, contrasting with a previously proposed "phonon liquid" picture^{3, 12} (see Supplementary Fig. 16 for more information). One noticeable change across the superionic transition is an increase in the scattering intensity over a broad Q and Q and Q are range (Figs. 3a,b), especially in the energy gap between the TA phonon peaks and elastic line, marked by the blue arrow in Figs. 3c,d (also see Supplementary Figs. 15f, 16 & 17). This accumulation of extra spectral

weight indicates a partial overdamping of the lattice phonon vibrations, developing into the QENS component discussed in Fig. 2, which was further confirmed with the constant-*Q* scans on the TAIPAN triple axis in Supplementary Fig. 18, similar analysis near the longitudinal phonons in Supplementary Fig. 19, as well as the MLMD simulation in the right panels in Figs. 3a,b (also see the discussion of Figs. 3e,f below). Importantly, we further observe that the diffuse scattering shows a strong *Q*-dependent modulation across reciprocal space, implying a coherent (concerted) diffusion mechanism (see Supplementary Section 5 for more information). This supports proposals that concerted collective hopping could favor fast diffusion in both ionic liquids and solid-state superionic conductors^{21, 33}.

To investigate the correlated dynamics of atoms occupying different crystallographic positions, we computed the partial phonon DOSs from our MLMD trajectories within the framework of the O structure (Figs. 3e,f). Interestingly, we find that the Ag and free Se (Se4 $_{\rm O}$ (2a) and Se5 $_{\rm O}$ (2a), corresponding to the Se2 $_{\rm C}$ (4c) and Se1 $_{\rm C}$ (4a) in the C structure) atoms exhibit strongly coupled phonon-like vibrations below $T_{\rm C}$ as both these atoms contribute significantly to the DOS around $E^{\sim}3$ meV, and that the partial phonon DOS of Ag at the elastic line (0 meV) is zero. However, the contribution from the free Se atoms above $T_{\rm C}$ is no longer prominent, indicating a decoupling of the correlated dynamics of Ag and free Se atoms. In addition, the partial phonon DOS from Ag (and to some extent that from free Se also) exhibits a non-zero contribution near 0 meV, further suggesting a partial overdamping of certain phonon modes and stochastic dynamics of the mobile Ag atoms hopping across its sublattice, which then brings about strong QENS signal and fill the energy gap of the TA phonon in Figs. 3b,d.

To further illustrate the importance of the strong correlation between the dynamics of Ag and free-Se atoms on the superionic transition, the mean squared displacements (MSD) evolving over time are calculated from the atomic trajectory as determined from MLMD simulation in three different scenarios: unconstrained lattice, frozen free Se4₀/Se5₀ atoms, and fully frozen host lattice (all Sn and Se atoms), respectively. At 300 K (below T_c), the MSD of Ag atoms remains constant over a long simulation time, revealing oscillations in a local potential energy minimum, independently of constraints on the host lattice (Fig. 3g, see Supplementary Fig. 22 for MSD of other atoms). On the other hand, the linear increase in MSD with time for Ag atoms develops at 400 K, characteristic of long-range diffusion, in the absence of constraints applied to the host lattice. However, and critically, we show that Ag diffusion becomes strongly suppressed by freezing the motions of Se4₀/Se5₀ atoms alone. This effect is of equal magnitude as achieved upon freezing the entire host lattice, as shown in Fig. 3h. This establishes a crucial role of free-Se atoms in enabling superionic Ag diffusion, in particular the intercluster jumps. In fact, a large shift in position and a huge increase in ADP of free-Se atoms above $T_{\rm C}$ was also established from our structural analysis in Supplementary Figs. 4-9, which further points to the importance of the dynamics of the free-Se atoms in enabling the superionic transition.

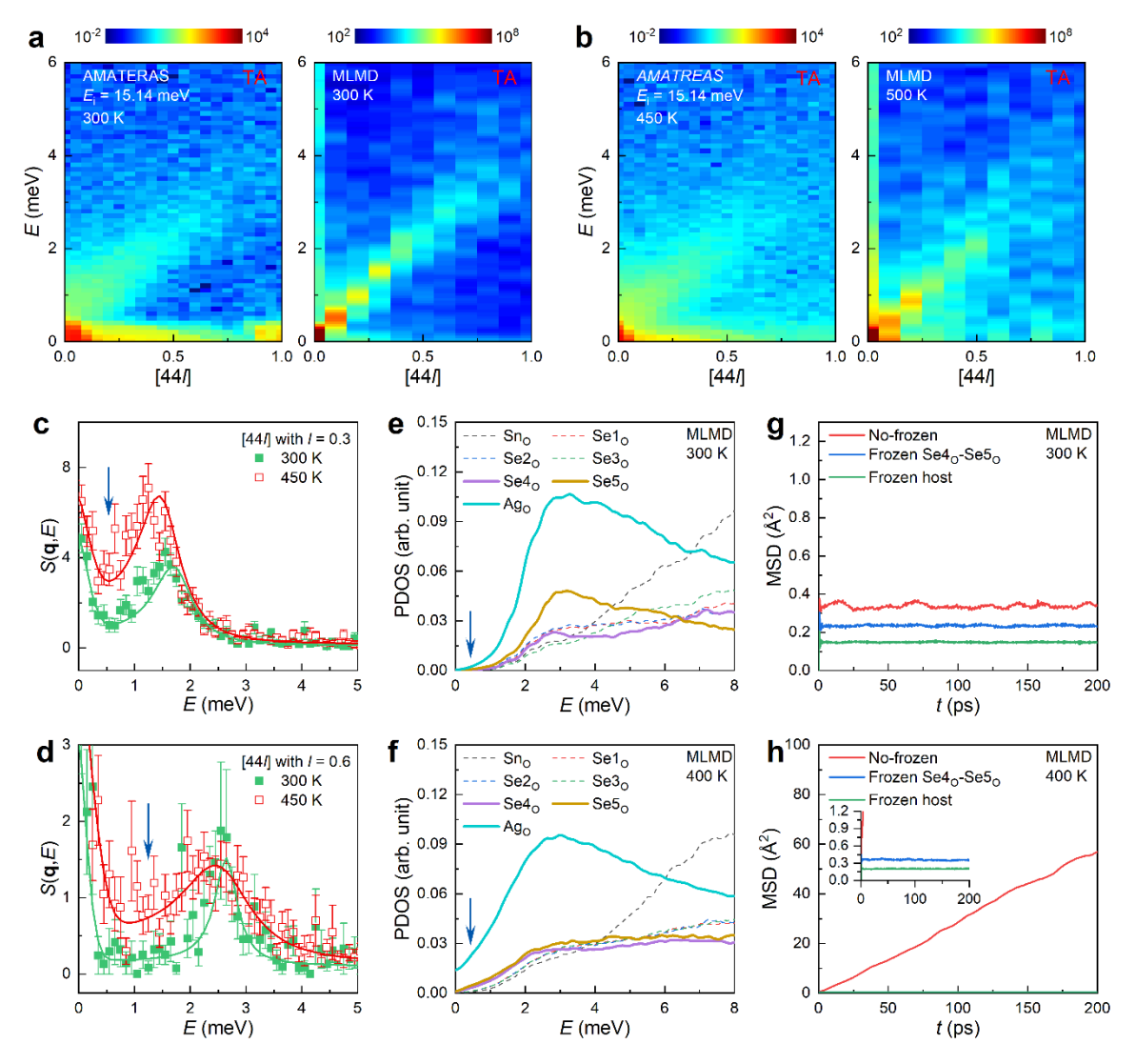


Fig. 3 Phonon dispersions and coupled vibrations of the Ag and free-Se atoms. a,b Transverse acoustic phonon (TA) dynamic structure factor, $S(\mathbf{q}, E)$, along [44/] directions as determined from INS measurement on AMATERAS with E_i = 15.141 meV at (a) 300 K and (b) 450 K, compared with the MLMD simulation (right panels in a and b). c,d, Constant-Q curves on the [44/] TA branch at the I values of (c) 0.3 r.l.u. and (d) 0.6 r.l.u., respectively. The solid lines are fits to damped harmonic oscillator (DHO) models (see Supplementary Fig. 16 for more details about the spectral fittings). Blue arrow marks an increase in scattering intensity within the 'energy gap'. e,f, Partial phonon density of states (PDOS) for each atoms around 3 meV calculated with MLMD within the frame work of the O structure at (e) 300 K and (f) 400 K. The arrows mark the PDOS change of the Ag sublattice near zero energy, indicating a partial phonon overdamping of the Ag sublattice which develops into a strong QENS signal and leads to an increase in the scattering intensity in (c,d). g,h, Evolution of the mean squared displacements for Ag atoms as functions of relaxation time as determined from the MLMD trajectories at (g) 300 K and (h) 400 K. Three different situations (no constrain, frozen Se4o/Se5o free atoms, and frozen host lattice) are considered.

Ultralow lattice thermal conductivity and extreme phonon anharmonicity. The persistence of TA phonon modes across the superionic phase transition, as demonstrated by the direct single-crystal INS measurement in Fig. 3a and Supplementary Fig. 16g, implies that the partial melting of the Ag sublattice is unlikely to be the dominant factor responsible for the ultralow lattice thermal conductivity, κ_{latt} , in the argyrodite-type superionic thermoelectrics. This is similar to the superionic (Ag,Cu)CrSe₂ compounds, where the picture of long-wavelength transverse acoustic phonon quasiparticles remains valid in the superionic phase^{7, 9}. In fact, the bulk transport measurements do not show any drop in κ_{latt} across the superionic transition, but rather a slight increase (Supplementary Fig. 23)^{30, 34, 35}. Therefore, intense phonon scattering already occurs far below $T_{\rm C}$. The dominant factors might be active across all temperatures so that κ_{latt} could be very low even near absolute zero degree, or they might sharply evolve with temperature causing a strong variation in κ_{latt} in the low-temperature range.

To unravel the mystery behind the ultralow κ_{latt} in the low temperature range, we carried out high-resolution INS measurements from 8 to 200 K on the AMATERAS spectrometer with E_i 7.738 meV. The S(Q,E) maps at three selective temperatures (8, 50 and 100 K) are shown in Fig. 4a-c, while the Bose-factor-corrected dynamic structure factors integrated over [1, 3.2] Å-1 (i.e. the dynamical susceptibility, χ'' , proportional to the phonon DOS divided by E) are shown in Fig. 4d. Clear acoustic streaks are seen arising from intense Bragg peaks over the whole temperature range. Several phonon bands are observed at 8 K in the range between 2 and 5 meV. However, these phonon bands broaden extremely quickly upon warming, coalescing into a featureless broad peak around ~3meV (similar to the data in Fig. 2) already at 50 K, an extremely low temperature in comparison with T_c . We note that this behavior is consistent with reported thermal conductivity measurements for Ag₈SnSe₆, which showed that κ_{latt} rises rapidly from 5K to ~15K, and then subsequently drops rapidly until ~50K, above which it becomes nearly invariant with temperature (Supplementary Fig. 23)^{30, 35}. The observed trend in χ'' , combined with the $\kappa_{\rm latt}(T)$ behavior, implies that argyrodite Ag₈SnSe₆ has a well-defined crystal structure below ~15 K with Ag ions vibrating in very shallow potential energy minima, but that extreme anharmonic phonon-phonon scattering rapidly develops on warming between acoustic phonons and lowenergy optical phonons, which causes a glass-like ultralow and nearly constant κ_{latt} above ~50K, well below T_c . Our MLMD simulations, which account for the full anharmonicity beyond third or fourth-order, qualitatively capture this fast evolution of phonon broadening on warming as shown in Fig. 4e (some observed deviations in the shape of computed spectra could arise from tiny differences in the potential energy landscape of Ag ions).

It is worth noting that the cut-off energy of acoustic phonons of Ag₈SnSe₆ argyrodites is ~2 times smaller than that of the typical clathrate and skutterudite "phonon-glass" systems^{36, 37} and then only possess a very limited Q-E momentum energy space for heat propagating acoustic phonon⁴. Additionally, its acoustic sound velocity is also ~2 to ~3 times smaller than the latter two systems³⁸. These two factors are also believed to make an important contribution to the suppression of κ_{latt} , although the INS data, as well as the bulk transport properties, suggest a dominant role of the extreme anharmonic phonon scatterings between the low-lying flat optical branches and acoustic branches.

On the other hand, the slight increase in κ_{latt} above the superionic transition indicates that κ_{latt} in Ag₈SnSe₆ is not merely attributed to phonon propagation but that an additional component develops^{30, 34, 35}. To model this effect, three κ contributions are considered: the propagation of phonons (virial), the convection term from superionic diffusion of Ag ions, as well as the interaction between lattice and convection (cross-term). The simulations were conducted

using the Green-Kubo equilibrium molecular dynamics (GK-EMD), and the results are shown in Supplementary Fig. 24 & Table 2. We find that phonon propagation dominates the thermal conductivity ($^{\circ}$ 0.2 W m $^{-1}$ K $^{-1}$) below $T_{\rm C}$, with the contributions from convection and cross-terms remaining negligible. In contrast, the partial melting of the Ag sublattice above $T_{\rm C}$ brings finite contributions from convection and cross processes. The positive contribution from $\kappa_{\rm latt}^{\rm cross}$ in the superionic phase signals a correlated behavior between the two heat transport channels of virial and convection. It is noted that the discrepancy between calculated thermal conductivity and reported value may arise from the grain boundary and defects in the sample preventing diffusion and convection term to the thermal conductivity.

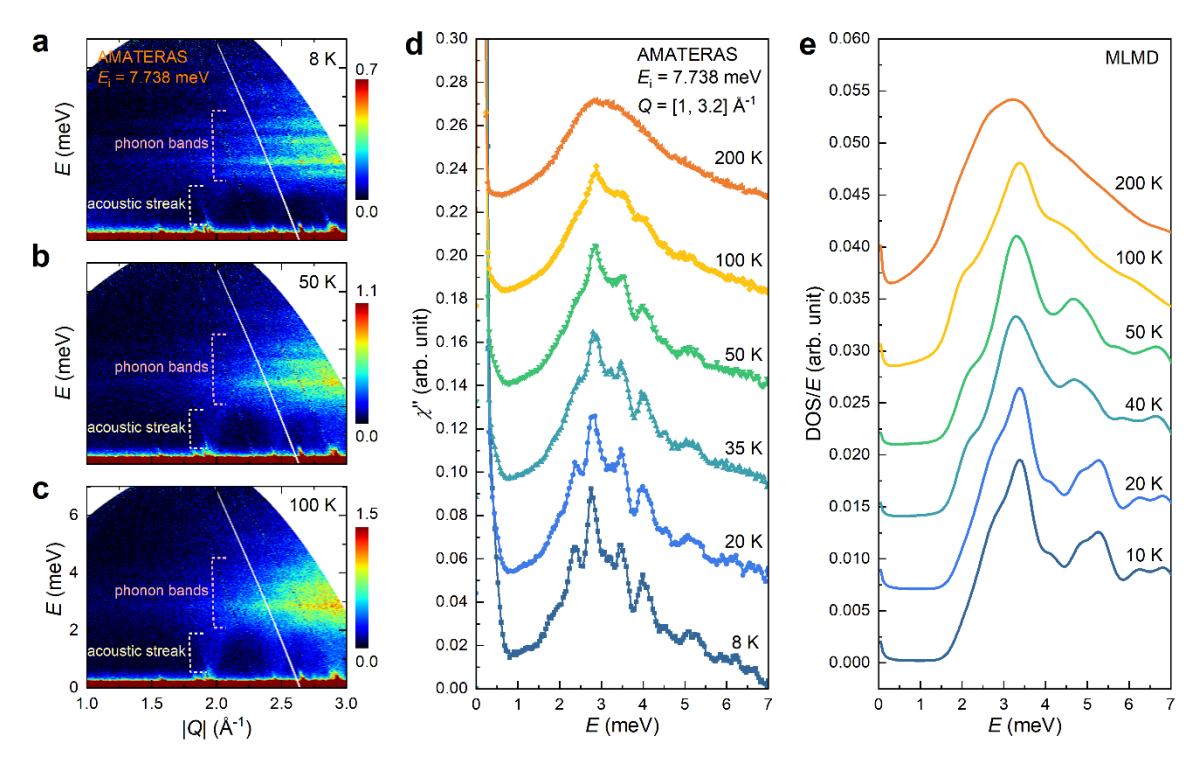


Fig. 4 Dramatic phonon broadening without energy softening at low temperature. a-c, S(Q,E) maps measured with E_1 = 7.738 MEV on AMATERAS at (a) 8 K, (b) 50 K, and (c) 100 K. The energy ranges for the acoustic phonon vertical streak and acoustic & optical phonon bands are marked with dashed lines. d, Bose-factor-corrected dynamic structure factor, χ'' , as integrated over the range $1 \le Q \le 3.2 \, \text{Å}^{-1}$ from 8 K to 200 K. The phonon bands present extremely quickly broadening with temperature (see Supplementary Section 6 for more information). e, Neutron-weighted DOS over energy transfer (DOS/E, equal to χ'') obtained from MLMD simulations at different temperatures.

Discussion

Previous studies of lattice dynamics in superionic materials have emphasized the importance of overall phonon anharmonicity but lacked more detailed data and analysis^{23, 25, 26}. In this work, we bring important new insights, revealing which specific phonon modes of the complex crystal framework control the gateway for the superionic transition. A key atomistic mechanism

underlying the superionic transition in Ag_8SnSe_6 involves the critical interaction between Ag and free-Se (4a and 4c Wyckoff positions in the cubic phase) sublattices, which both feature low-frequency vibrations in very shallow potential energy minima. The increasingly strong effect of these shallow anharmonic potentials occurs well below T_c , revealed as phonon broadening and softening, and ultimately leads to a decoupled dynamic behavior between the intercorrelated Ag and free-Se sublattice at T_c , as the Ag ions eventually become disanchored from the anionic framework. For instance, this important insight could explain why the modification of S at the 4a and 4c Wyckoff positions in Li_6PS_5X (X = CI, Br, I), the same crystallographic sites as the free Se atoms in high-T cubic Ag_8SnSe_6 , are effective in improving the ionic conductivity, either by doping halides and rotational cyanide or by introducing site disordering^{20, 25, 39}. These chemical substitution might weaken the correlation between the cations and the free-atoms and decouple the correlated dynamics above T_c , which is in contrast to the paddle-wheel mechanism where strong correlation between translational motion of cations and rotation of anion-polyhedra needs to be preserved during the superionic transition $^{40, 41}$.

We find that the superionic transition does not suppress the long-wavelength transverse acoustic phonons in Ag₈SnSe₆, similar to reports in structurally simpler compounds (Ag,Cu)CrSe₂ and Cu₂Se⁷⁻⁹. Rather, a quick development of extreme phonon anharmonicity dramatically suppresses the lattice thermal conductivity at temperatures ~10x lower than T_c , and leads to the ultralow κ_{latt} even at ~50 K. On the way to pursuing a lower lattice thermal conductivity, one could therefore focus on the intrinsic phonon anharmonicity and weak bonding rather than the fast ionic diffusion itself^{9, 31}. In fact, the presence of long-distance superionic diffusion actually increases thermal transportation via convection, and may undermine the chemical stabilities of superionic thermoelectric materials^{35, 42}. Therefore, practical exploration of superionic thermoelectric materials should focus on the phases below the superionic transition temperature, e.g. try to improve the stability of this phase⁴³. Otherwise, the key phonon modes should be recognized so as to take some targeted methods to raise the diffusion barrier⁴⁴. In the case of argyrodites, the effective means might be to tune the free 4a and 4c Wyckoff positions as suggested by the different ionic conductivities in Li₆PS₅X (X = Cl, Br, I) superionic conductors²⁰. To summarize, through a combined SXRD, SCND, INS, QENS measurements and MLMD simulations, we revealed key mechanisms underlying the intricate phonon-ion interactions in topical superionic materials, in which the traditional quasiharmonic phonon picture is insufficient. These fundamental insights are expected to facilitate the design of novel materials as thermoelectrics for energy conversion or as solid-state electrolytes for energy storage.

References

- Zhang, Z. & Nazar, L. F. Exploiting the paddle-wheel mechanism for the design of fast ion conductors. *Nat. Rev. Mater.* 7, 389-405 (2022).
- 2. Kamaya, N., et al. A lithium superionic conductor. Nat. Mater. 10, 682-686 (2011).
- 3. Liu, H., et al. Copper ion liquid-like thermoelectrics. Nat. Mater. 11, 422-425 (2012).

- 4. Lin, S., et al. High Thermoelectric Performance of Ag₉GaSe₆ Enabled by Low Cutoff Frequency of Acoustic Phonons. Joule 1, 816-830 (2017).
- 5. Zhao, K., et al. Recent Advances in Liquid-Like Thermoelectric Materials. Adv. Funct. Mater. 30, 1903867 (2019).
- 6. Li, W., et al. Crystal Structure Induced Ultralow Lattice Thermal Conductivity in Thermoelectric Ag₉AlSe₆. Adv. Energy Mater. **8**, 1800030 (2018).
- 7. Niedziela, J. L., et al. Selective breakdown of phonon quasiparticles across superionic transition in CuCrSe₂. *Nat. Phys.* **15**, 73-78 (2019).
- 8. Voneshen, D. J., et al. Hopping Time Scales and the Phonon-Liquid Electron-Crystal Picture in Thermoelectric Copper Selenide. *Phys. Rev. Lett.* **118**, 145901 (2017).
- 9. Ding, J., et al. Anharmonic lattice dynamics and superionic transition in AgCrSe₂. Proc. Natl. Acad. Sci. U.S.A. 117, 3930-3937 (2020).
- 10. Qiu, W., et al. Part-crystalline part-liquid state and rattling-like thermal damping in materials with chemical-bond hierarchy. *Proc. Natl. Acad. Sci. U.S.A.* **111**, 15031-15035 (2014).
- 11. Li, L., et al. High thermoelectric performance of superionic argyrodite compound Ag₈SnSe₆. J. Mater. Chem. C 4, 5806-5813 (2016).
- 12. Li, B., et al. Liquid-like thermal conduction in intercalated layered crystalline solids. *Nat. Mater.* **17**, 226-230 (2018).
- 13. Trachenko, K. Heat capacity of liquids: An approach from the solid phase. *Phys. Rev. B* 78, 104201 (2008).
- 14. Janek, J. & Zeier, W. G. A solid future for battery development. Nat. Energy 1, 16141 (2016).
- 15. Famprikis, T., et al. Fundamentals of inorganic solid-state electrolytes for batteries. *Nat. Mater.* **18**, 1278-1291 (2019).
- 16. Zhang, B., et al. Mechanisms and properties of ion-transport in inorganic solid electrolytes. Energy Storage Mater. 10, 139-159 (2018).
- 17. Wang, C., *et al.* Ion Hopping: Design Principles for Strategies to Improve Ionic Conductivity for Inorganic Solid Electrolytes. *Small* **18**, 2107064 (2022).
- 18. Bachman, J. C., et al. Inorganic Solid-State Electrolytes for Lithium Batteries: Mechanisms and Properties Governing Ion Conduction. Chem. Rev. 116, 140-162 (2015).
- 19. Krauskopf, T., Culver, S. P. & Zeier, W. G. Bottleneck of Diffusion and Inductive Effects in Li₁₀Ge_{1-x}Sn_xP₂S₁₂. *Chem. Mater.* **30**, 1791-1798 (2018).

- 20. Hogrefe, K., et al. Opening Diffusion Pathways through Site Disorder: The Interplay of Local Structure and Ion Dynamics in the Solid Electrolyte Li_{6+x}P_{1-x}Ge_xS₅I as Probed by Neutron Diffraction and NMR. J. Am. Chem. Soc. **144**, 1795-1812 (2022).
- 21. He, X., Zhu, Y. & Mo, Y. Origin of fast ion diffusion in super-ionic conductors. *Nat. Commun.* **8**, 15893 (2017).
- 22. Canepa, P., et al. High magnesium mobility in ternary spinel chalcogenides. Nat. Commun. 8, 1759 (2017).
- 23. Muy, S., et al. Phonon–Ion Interactions: Designing Ion Mobility Based on Lattice Dynamics. Adv. Energy Mater. **11**, 2002787 (2021).
- 24. Gao, Y., et al. Classical and Emerging Characterization Techniques for Investigation of Ion Transport Mechanisms in Crystalline Fast Ionic Conductors. Chem. Rev. 120, 5954-6008 (2020).
- 25. Kraft, M. A., et al. Influence of Lattice Polarizability on the Ionic Conductivity in the Lithium Superionic Argyrodites Li₆PS₅X (X = Cl, Br, I). J. Am. Chem. Soc. **139**, 10909-10918 (2017).
- 26. Muy, S., et al. Tuning mobility and stability of lithium ion conductors based on lattice dynamics. Energy Environ. Sci. 11, 850-859 (2018).
- 27. Gupta, M. K., et al. Fast Na diffusion and anharmonic phonon dynamics in superionic Na₃PS₄. Energy Environ. Sci. **14**, 6554-6563 (2021).
- 28. Gupta, M. K., et al. Soft-phonon anharmonicity, floppy modes, and Na₃FY (Y = S,Se,Te): Ab initio and machine-learned molecular dynamics simulations. *Phys. Rev. B* **106**, 014311 (2022).
- 29. Gupta, M. K., *et al.* Strongly Anharmonic Phonons and Their Role in Superionic Diffusion and Ultralow Thermal Conductivity of Cu₇PSe₆. *Adv. Energy Mater.* **12**, 2200596 (2022).
- 30. Bernges, T., et al. Considering the Role of Ion Transport in Diffuson-Dominated Thermal Conductivity. Adv. Energy Mater. 12, 2200717 (2022).
- 31. Lin, S., Li, W. & Pei, Y. Thermally insulative thermoelectric argyrodites. Mater. Today 48, 198-213 (2021).
- 32. Sakata, M. & Sato, M. Accurate structure analysis by the maximum-entropy method. *Acta Crystallogr. Sec. A* **46**, 263-270 (1990).
- 33. Burankova, T., et al. Collective Ion Diffusion and Localized Single Particle Dynamics in Pyridinium-Based Ionic Liquids. J. Phys. Chem. B 118, 14452-14460 (2014).
- 34. Jin, M., et al. Fabrication and Thermoelectric Properties of Single-Crystal Argyrodite Ag₈SnSe₆. Chem. Mater. **31**, 2603-2610 (2019).
- 35. Zhang, X., et al. Thermoelectric properties of n-type Nb-doped Ag₈SnSe₆. J. Appl. Phys. 119, 135101 (2016).
- 36. Christensen, M., et al. Avoided crossing of rattler modes in thermoelectric materials. *Nat. Mater.* **7**, 811-815 (2008).

- 37. Koza, M. M., et al. Breakdown of phonon glass paradigm in La- and Ce-filled Fe₄Sb₁₂ skutterudites. *Nat. Mater.* **7**, 805-810 (2008).
- 38. Chen, Z., et al. Rationalizing phonon dispersion for lattice thermal conductivity of solids. *National Science Review* **5**, 888-894 (2018).
- 39. Maughan, A. E., *et al.* Lowering the Activation Barriers for Lithium-Ion Conductivity through Orientational Disorder in the Cyanide Argyrodite Li₀PS₅CN. *Chem. Mater.* **33**, 5127-5136 (2021).
- 40. Fang, H. & Jena, P. Argyrodite-type advanced lithium conductors and transport mechanisms beyond peddle-wheel effect. *Nat. Commun.* **13**, 2078 (2022).
- 41. Smith, J. G. & Siegel, D. J. Low-temperature paddlewheel effect in glassy solid electrolytes. *Nat. Commun.* **11**, 1483 (2020).
- 42. Dennler, G., et al. Are Binary Copper Sulfides/Selenides Really New and Promising Thermoelectric Materials? Adv. Energy Mater. 4, 1301581 (2014).
- 43. Jood, P., Chetty, R. & Ohta, M. Structural stability enables high thermoelectric performance in room temperature Ag₂Se. *J. Mater. Chem. A* **8**, 13024-13037 (2020).
- 44. Mao, T., et al. Enhanced Thermoelectric Performance and Service Stability of Cu2Se Via Tailoring Chemical Compositions at Multiple Atomic Positions. *Adv. Funct. Mater.* **30**, 1908315 (2020).

Methods

Sample synthesis. Large single-crystal ingots of Ag₈SnSe₆ were synthesized using a vertical Bridgman method³⁴. High purity Ag, Sn, and Se elements (>99.99%) were weighted according to the stoichiometric ratio. The mixture of the starting materials was loaded into a quartz ampoule (25 mm diameter) and flame sealed under vacuum at ~10⁻³ Pa. The sealed ampoule was placed into a 1273 K rocking furnace, and sample homogeneity was achieved by a 30-min rocking motion with a rate of 20 rpm. Then the furnace was cooled to room temperature naturally. The obtained polycrystalline ingot was placed into a Bridgman furnace. The single crystal growth conditions were set at 1123 K with a temperature gradient of 5-8 K cm⁻¹ and a lowering rate of 1.5 mm h⁻¹. The as-gown crystal ingot was cooled to room temperature with a rate of 20-25 K h⁻¹. Finally, quasi-single-domain crystals were cut from the ingot for single crystal measurements (Supplementary Fig. 1a) and powder samples were obtained by grinding the pieces from the same ingot. The crystal alignments were conducted with an X-ray back reflection Laue diffractometer, Multiwire Laboratories MWL120. One of the Laue patterns is shown in Supplementary Fig. 1b.

Characterization of crystal structures. Synchrotron X-ray diffraction (SXRD). The SXRD patterns were collected on the Powder Diffraction beamline at the Australian Synchrotron with a wavelength of 0.6881 Å as calibrated with the standard reference material of LaB₆. 5 mg of finely and uniformly ground powders were loaded into the borosilicate capillaries (diameter \approx 0.3 mm) and the capillaries are rotated to improve powder averaging during data collection. The measurements were carried out from 90 K to 450 K at steps of 10 K near the phase transition temperature and 30 K far away from the phase transition temperature. Each pattern over the range 3° < 20 < 77.8° was collected for 10 min. The obtained patterns were analyzed using the Rietveld refinement methods with the FullProf suite⁴⁵.

Single crystal neutron diffraction (SCND). Single crystal SCND data was collected on the Hot Neutron Four-Circle Diffractometer, D9, at the Institut Laue-Langevin (ILL) at a wavelength of 0.837 Å. A 3 × 3.5 × 3 mm single crystal of Ag₈SeSn₆ was used for the measurements. The integrated intensities of all accessible reflections within $sin \theta / \lambda < 0.75$ and 1.15 Å⁻¹ were measured at two temperature points, 300 K (below T_c) and 400 K (above T_c), leading to 1307 and 357 unique reflections, respectively. The data was analyzed using the integrated intensity refinement method with the FullProf suite⁴⁵. Then, the nuclear density distributions were analyzed from the observed structure factor by means of the maximum entropy method (MEM) based on the Dysnomia program^{32, 46}. The crystal structures and the nuclear density distribution isosurfaces are visualized using VESTA⁴⁷. In addition, the diffuse pathways and their potential profile are calculated with bond valence site energy (BVSE) method using the program of SoftBV⁴⁸ (see Supplementary Fig. 9).

Inelastic neutron scattering measurements. Measurements on powder sample. Inelastic neutron scattering (INS) measurements on the cold neutron time-of-flight spectrometer, TOFTOF, at the Heinz Maier-Leibnitz Zentrum (MLZ)⁴⁹ and the Cold-Neutron Disk-Chopper Spectrometer, BL14 AMATERAS, at the Materials and Life Science Experimental Facility (MLF) of J-PARC^{50, 51}. The TOFTOF instrument was configured with an incident neutron wavelength of 3 Å, affording an incident energy of 9.09 meV with an instrumental resolution of ~0.31 meV at the elastic line. ~14 g Ag₈SnSe₆ powder sample are sealed in a thin-walled Al can of a 22.5 diameter. A series spectrum was measured at T = 150, 250, 300, 350, 360, 410, 480 and 550 K. The data was reduced with the Mantidplot software⁵², and then visualized and analyzed with the Data Analysis and Visualization Environment (DAVE)⁵³. In the AMATERAS measurements, the incident energies of $E_i = 7.738$ and

3.136 meV was used, which offer better energy resolutions of \sim 0.226 and \sim 0.061 meV, respectively. \sim 5 g powder sample were sealed in a thin-walled Al can with a diameter of 14 mm. The measurements are carried at 8, 20, 35, 50, 100, 200, 300, 400 and 500 K. The collected spectra were visualized with the Utsusemi suite⁵¹. Phonon density of states (DOSs) could be obtained by integrating the S(Q,E) over a broad Q range⁵⁴:

$$g(E) = A \times \langle 4M \frac{\exp(2W)}{\hbar^2 Q^2} \frac{E}{n(E,T) + \frac{1}{2} \pm \frac{1}{2}} S(Q,\omega) \rangle \tag{1}$$

where A is a scaling factor, M is the atomic mass, $\exp(2W)$ is the Debye-Waller factor, and n(E,T) is the Bose occupation factor, while the '+' and '–' signs denote energy loss or energy gain of neutrons, respectively. The brackets $\langle \cdots \rangle$ represent an average operator over all Q range at a given energy. Within a polyatomic material, different elements have different scattering cross sections σ and atomic masses M, and this would cause a deviation from the real phonon DOSs but give a neutron-weighted phonon DOS^{54, 55}:

$$g_{\text{NW}}(E) = \sum_{i} f_{i} \frac{\sigma_{i}}{M_{i}} g_{i}(E) \exp(-2W_{i})$$
 (2)

i denotes different elements, f_i represent the atomic concentration, and $g_i(E)$ is the real partial phonon DOS of the element i. Then the dynamical susceptibility, χ'' can be obtained with the following formula as

$$\chi'' = \frac{S(Q, \omega)}{n(E, T) + \frac{1}{2} \pm \frac{1}{2}}.$$
 (3)

Measurements of phonon dispersions with single crystal. INS measurements on the Ag_8SnSe_6 single crystal with AMATERAS spectrometer. The chopper configuration was carefully set and multi-incident energies of E_i = 15.141 and 7.734 meV were selected with different energy resolutions of 0.53 and 0.197 meV. The crystal was measured in the (*HHL*) plane with a 0.5° rotation step along the vertical axis of [1-10] axis (Supplementary Fig. 1), and the (440), (331) and (33-1) Brillouin zones are covered. The data were collected at two different temperatures at 300 and 450 K, and combined to form the four-dimensional scattering function, $S(\mathbf{Q}, E)$, using the Utsusemi suite, which were then sliced along selected \mathbf{Q} -directions to visualize the two-dimensional data using D4MatSlicer function of Utsusemi suite⁵¹. One-dimensional cutting curves along the energy axis at specific \mathbf{Q} points are also extracted and then fitted using the PAN module as built-in the DAVE program⁵³. To acquire further information on the phonon dispersion, we also carried out INS measurements at selective momentum spaces on the thermal triple axis spectrometer, TAIPAN, at the Australian Centre for Neutron Scattering (ACNS), Australian Nuclear Science and Technology Organisation (ANSTO)⁵⁶. The final energy, E_f , was fixed as 14.87 meV with pyrolytic graphite filters, monochromators and analyzers.

Theoretical simulations. Ab initio molecular dynamics simulations. The first-principles lattice dynamics and ab initio molecular dynamics (AIMD) simulations were performed within the planewave density functional theory (DFT) framework, as implemented in the Vienna ab initio simulation package (VASP)⁵⁷. The calculations used the projector augmented wave (PAW) formalism within generalized the gradient approximation (GGA) parameterization by Perdew, Becke, and Ernzerhof (PBE)^{58, 59}. A plane wave kinetic energy cutoff of 400 eV and k-point sampling of 4×4×2, using the Monkhorst-Pack method, was used⁶⁰. The self-consistent convergence

threshold for electronic minimization was set to 10^{-8} eV. The lattice parameters and atomic positions of the structure were optimized until the forces on individual atoms were less than 1 meV/Å.

Harmonic phonon calculations were performed for the low-T orthorhombic phase ($Pmn2_1$) using a 2×2×2 supercell (240 atoms) and displacement amplitudes of 0.01 Å with the software Phonopy⁶¹. The total energy and atomic forces were calculated on 52 distinct displacement configurations for the orthorhombic phase. The phonon calculations in the superionic cubic phase were not possible within this approach due to partial Ag site occupancies and extreme anharmonicity. Instead, we computed phonon spectral energy density directly from MD trajectories (see below).

Machine-learned molecular dynamics. The AIMD simulation also used a $2\times2\times2$ supercell of the orthorhombic phase (240 atoms). The Brillouin zone center-only (Γ point) electronic k-point and an energy convergence of 10^{-6} eV were used to integrate the trajectories. We employed the NVT ensemble and ran the AIMD simulation for 10-12 ps with a time step of 2 fs. The temperature of the system was controlled by a Nosé–Hoover thermostat. Data from the first 2 ps were used for equilibration purposes.

We used the DEEPMD $code^{62}$ based on a neural network algorithm to generate a neural network force-field that reproduces as best as possible the AIMD dynamics. The AIMD dataset (energies, forces, and virials from 100 K to 700 K with an interval of 100 K) was used for training the neural network force-field. A cutoff of 8.0 Å for neighbor atom interaction and the embedding and fitting network size is set to (25, 50, 100) and (240, 240, 240), respectively. The generated force field was used to compute various thermodynamic quantities (pair distribution function (PDF), phonon density of state (DOS), and mean squared displacement (MSD)) and checked against AIMD results. We found an excellent agreement between the machine-learned molecular dynamics (MLMD) and AIMD results. The MD software package LAMMPS was then used for classical simulations using the machine-learned force-field. These MLMD simulations were performed on a 2×2×2 supercell of superionic cubic phase (480 atoms) over trajectories of 1 nanosecond duration (with a time step of 1 fs) within an NVT ensemble (constant particles, volume, and temperature). These extensive simulations provide momentum and energy resolutions of ~0.1 Å-¹ and ~10 μ eV, respectively. Such fine resolution is essential to access the QENS spectrum through simulations.

The phonon DOS and diffusion coefficients were obtained from LAMMPS trajectories. The partial $g_j(\omega)$ and total phonon DOS $g(\omega)$ was obtained by Fourier transformation of the velocity autocorrelation function as:

$$g_j(\omega) = \int e^{i\omega t} \langle v_j(t) | v_j(0) \rangle dt$$
 (4)

$$g(\omega) = \sum_{i} g_{j}(\omega) \tag{5}$$

where $v_j(t)$ is the j^{th} atom position at time t, and the symbol $\langle \cdots \rangle$ indicates an ensemble average over atoms. Using the calculated phonon density of states one can also compute the dynamical structure factor of j^{th} element, $S_j(\omega)$ given as:

$$S_{j}(\omega) = g_{j}(\omega) \frac{n(\omega, T)}{\omega} \tag{6}$$

The MSD of j^{th} species, $\langle u_i^2(t) \rangle$, is at time t is estimated as:

$$\langle u_j^2(t) \rangle = \frac{1}{N_j} \sum_{j=1}^{N_j} \langle \left| r_j(t) - r_j(0) \right|^2 \rangle \tag{7}$$

Here $r_j(\tau)$ is the j^{th} atom position at time t, and N_j is the total number of atoms of element j in the simulation cell. The isotropic diffusion coefficient (D) of j^{th} element was estimated as:

$$D = \langle u_i^2(t) \rangle / 6\tau \tag{8}$$

The MSD of k^{th} atom, $\langle u_k^2(t) \rangle$ contributed from phonons of energy E in the Brillouin zone is given by:

$$\langle u_k^2(t)\rangle = \int (n + \frac{1}{2}) \frac{\hbar}{m_k E} g_k(E) dE \tag{9}$$

Where $n = \left[\exp\left(\frac{E}{k_{\mathrm{B}}T}\right) - 1\right]^{-1}$, $g_k(E_{q,v})$, and m_k is the partial density of states and mass of the k^{th} atom in the unit cell. This infers that the atoms with a large partial density of states at low energies will have large MSD.

To investigate the mode and direction resolved phonon anharmonicity, we have performed the spectral energy density calculation. It is important to note that the quasiharmonic approximation and perturbation theory which treats only third or fourth-order expansion of free energy, fails for a strongly anharmonic system. Hence, we performed phonon SED calculation to account for the full anharmonicity and their impact on phonon energy. The phonon spectral energy density at the wavevector \vec{q} and energy E is defined as⁶³:

$$\varphi(\vec{q}, E) = \frac{1}{4\pi\tau_0 N} \sum_{\alpha, k} m_k \left| \sum_{n=1}^{N} \int_0^{t_0} \overrightarrow{u}_{\alpha} \binom{n}{k}; t \right| \exp\left[i\vec{q}.\vec{r} \binom{n}{k} - iEt/\hbar\right] dt \right|^2$$
(10)

where N is the number of unit-cells in a supercell ($N=N_1\times N_2\times N_3$), summation index α runs over Cartesian x, y, and z; index k runs over the number of particles in the unit cell. m_k , $\vec{r} \binom{n}{k}$ are mass of k^{th} atom and its equilibrium position in the n^{th} unit cell, and $\overrightarrow{u}_{\alpha}\binom{n}{k}$; t) is the velocity of k^{th} atom in the n^{th} unit cell at time t. An MD simulation with a supercell dimension ($N_1\times N_2\times N_3$) and trajectory length of t_0 ps gives an energy and momentum resolution of ΔE =4.136/ t_0 meV and $\Delta \vec{q} = \frac{2\pi}{aN_1}\hat{t} + \frac{2\pi}{aN_2}\hat{f} + \frac{2\pi}{aN_3}\hat{k}$, respectively. Here a is the lattice parameter of the cubic cell.

Thermal conductivity. The thermal conductivity across the superionic transition were calculated using the equilibrium molecular dynamics (EMD) and the Green-Kubo formalism, based on the MLMD as validated above. This method treats all orders of anharmonicity in materials and also able us to estimate the phononic and non-phononic contribution to lattice thermal-conductivity as a function of time. The heat-flux, J(t) is given by:

$$J(t) = \sum_{i} v_{i} \varepsilon_{i} + \frac{1}{2} \sum_{i:i \neq i} r_{ij} \left(F_{ij} \cdot v_{i} \right)$$

$$\tag{11}$$

where v_i and ε_i are the velocity and energy of the i^{th} particle. F_{ij} is the force between i^{th} and j^{th} atoms. The first and second terms in Equation (11) represent the convection and conduction term of heat flux, respectively. Convection results from the mass transport of mobile (diffusive) species, while the second term describes the energy exchange due to interatomic interactions, e.g., lattice vibrations in crystalline solids. In the Green-Kubo formalism, the total lattice thermal conductivity, κ_{latt} , is expressed as a time integral of the heat current autocorrelation function (HCACF)⁶⁴:

$$\kappa_{\text{latt}} = \frac{1}{k_{\text{B}}T^{2}V} \left[\int_{0}^{t} \langle J_{\text{virial}}(0)J_{\text{virial}}(t) \rangle t + \int_{0}^{t} \langle J_{\text{conv}}(0)J_{\text{conv}}(t) \rangle dt + 2 \int_{0}^{t} \langle J_{\text{virial}}(0)J_{\text{conv}}(t) \rangle dt \right]$$

$$(12)$$

The three terms in the square bracket represent the contributions to $\kappa_{\rm total}$ from solid-like phononic vibrations ($\kappa_{\rm latt}^{\rm virial}$), non-phononic convection of liquid-like Ag atoms ($\kappa_{\rm latt}^{\rm conv}$) and cross interactions between liquid-like and solid-like contributions ($\kappa_{\rm latt}^{\rm cross}$), respectively. In the calculation, we used a supercell of a 6×6×4 supercell of orthorhombic phase (42000 atoms). We first equilibrated the system within the NVT ensemble and then used NVE (constant particles, volume, and energy) for heat-flux calculation for about 1-2 ns with a timestep of 1 fs.

Data availability

The data that support the findings of this study are available from the corresponding author upon request.

References

- 32. Sakata, M. & Sato, M. Accurate structure analysis by the maximum-entropy method. *Acta Crystallogr. Sec. A* **46**, 263-270 (1990).
- 34. Jin, M., et al. Fabrication and Thermoelectric Properties of Single-Crystal Argyrodite Ag₈SnSe₆. Chem. Mater. **31**, 2603-2610 (2019).
- 45. Rodríguez-Carvajal, J. Recent advances in magnetic structure determination by neutron powder diffraction. *Physica B* **192**, 55-69 (1993).
- 46. Momma, K., et al. Dysnomia, a computer program for maximum-entropy method (MEM) analysis and its performance in the MEM-based pattern fitting. *Powder Diffr.* **28**, 184-193 (2013).
- 47. Momma, K. & Izumi, F. VESTA 3 for three-dimensional visualization of crystal, volumetric and morphology data. *J. Appl. Crystallogr.* **44**, 1272-1276 (2011).
- Wong, L. L., et al. Bond Valence Pathway Analyzer—An Automatic Rapid Screening Tool for Fast Ion Conductors within softBV. Chem. Mater. 33, 625-641 (2021).

- 49. Lohstroh, W. & Evenson, Z. TOFTOF: Cold neutron time-of-flight spectrometer. *J. Large Scale Res. Facil.* **1**, 15 (2015).
- Nakajima, K., et al. Recent Update of AMATERAS: A Cold-Neutron Disk-Chopper Spectrometer. JPS Conf. Proc. 33, 011089 (2021).
- 51. Inamura, Y., et al. Development Status of Software "Utsusemi" for Chopper Spectrometers at MLF, J-PARC. J. Phys. Soc. Jpn. 82, SA031 (2013).
- 52. Arnold, O., et al. Mantid—Data analysis and visualization package for neutron scattering and μ SR experiments. Nucl. Instrum. Methods Phys. Res., Sect. A **764**, 156-166 (2014).
- 53. Azuah, R. T., et al. DAVE: A Comprehensive Software Suite for the Reduction, Visualization, and Analysis of Low Energy Neutron Spectroscopic Data. J. Res. Natl. Inst. Stand. Technol. 114, 341-358 (2009).
- 54. Ren, Q., et al. Ultrasensitive barocaloric material for room-temperature solid-state refrigeration. *Nat. Commun.* **13**, 2293 (2022).
- 55. Ren, Q., et al. Establishing the carrier scattering phase diagram for ZrNiSn-based half-Heusler thermoelectric materials. *Nat. Commun.* **11**, 3142 (2020).
- 56. Danilkin, S. A., et al. The TAIPAN thermal triple-axis spectrometer at the OPAL reactor. *J. Neutron Res.* **15**, 55-60 (2007).
- 57. Kresse, G. & Furthmüller, J. Efficiency of ab-initio total energy calculations for metals and semiconductors using a plane-wave basis set. *Comput. Mater. Sci.* **6**, 15-50 (1996).
- 58. Perdew, J. P., Burke, K. & Ernzerhof, M. Generalized Gradient Approximation Made Simple [Phys. Rev. Lett. 77, 3865 (1996)]. *Phys. Rev. Lett.* **78**, 1396-1396 (1997).
- 59. Kresse, G. & Joubert, D. From ultrasoft pseudopotentials to the projector augmented-wave method. *Phys. Rev. B* **59**, 1758-1775 (1999).
- 60. Monkhorst, H. J. & Pack, J. D. Special points for Brillouin-zone integrations. *Phys. Rev. B* 13, 5188-5192 (1976).
- 61. Togo, A. & Tanaka, I. First principles phonon calculations in materials science. *Scripta Mater.* **108**, 1-5 (2015).
- 62. Wang, H., et al. DeePMD-kit: A deep learning package for many-body potential energy representation and molecular dynamics. *Comput. Phys. Commun.* 228, 178-184 (2018).
- 63. Thomas, J. A., et al. Predicting phonon dispersion relations and lifetimes from the spectral energy density. *Phys. Rev. B* **81**, 081411 (2010).
- 64. Zhou, Y., et al. Thermal transport crossover from crystalline to partial-crystalline partial-liquid state. *Nat. Commun.* **9**, 4712 (2018).

Acknowledgements

Q.Y.R. thanks the project from Guangdong Basic and Applied Basic Research Foundation (Grant No. 2021B1515140014), National Natural Science Foundation of China (Grant No. 52101236), the Institute of High Energy Physics, Chinese Academy of Science (Grant No. E15154U110), and Open project of Key Laboratory of Artificial Structures and Quantum Control (Ministry of Education) (Grant No. 2021-05). J.M. thanks the financial support from the National Science Foundation of China (No. U1732154). J.D. and O.D. were supported by the U.S. National Science Foundation DMREF award DMR-2119273. Y.Z.P. thanks the support from the National Science Foundation of China (No. T2125008). M.J. thanks the financial support from the National Science Foundation of China (Grant No. 52272006) and "Shuguang Program" from Shanghai Education Development Foundation and Shanghai Municipal Education Commission. Z.X.C. thanks Australia Research Council for support (DP210101436). Q.Y.R. thanks Dr. Yanfeng Guo and Dr. Hao Su from ShanghaiTech University for the help on crystal alignment, and Dr. Sergey Danilkin, Dr. Dehong Yu and Dr. Chin-Wei Wang from ANSTO for the assistance of the neutron data collection. All authors acknowledge the beam time granted by ILL (Proposal Nos. 5-14-263 and 5-14-268), FRM-II (Proposal No. 14754), J-PARC (Proposal Nos. 2018B0262 and 2020A0228), ANSTO (Proposal Nos. P7875) and technical support from the instrument scientists during the experiments at the Australian Synchrotron.

Author contributions

Q.Y.R, O.D., and J.M. conceived the project. M.J., Z.W.C., S.Q.L. and Y.Z.P. prepared the single crystal samples, and Q.Y.R. aligned the crystals with the help from G.H.W. J.L.W. and Z.X.C. performed the synchrotron x-ray diffraction measurements, and the results were analyzed by Q.Y.R. Q.Y.R. carried out the single crystal neutron measurements and structural analyses with the help from J.T.W., O.F. and J.A.R.V. Neutron scattering measurements were conducted by Q.Y.R., M.K., K.N., M.W., F.Z. and J.T.W. and were analyzed by Q.Y.R. with assistance from X.T. and J.M. M.K.G., J.X.D. and O.D. performed the first-principle and machine-learned molecular dynamic simulations. Q.Y.R. drafted the manuscript. All authors edited and finalized the manuscript.

Competing interests

The authors declare no competing interests.